ACS APPLIED MATERIALS & INTERFACES

www.acsami.org

Research Article

# Schottky Contacts on Polarity-Controlled Vertical ZnO Nanorods

Alex M. Lord,* Vincent Consonni, Thomas Cossuet, Fabrice Donatini, and Steve P. Wilks

Cite This: *ACS Appl. Mater. Interfaces* 2020, 12, 13217−13228

Read Online

ACCESS | Metrics & More | Article Recommendations | Supporting Information

**ABSTRACT:** Polarity-controlled growth of ZnO by chemical bath deposition provides a method for controlling the crystal orientation of vertical nanorod arrays. The ability to define the morphology and structure of the nanorods is essential to maximizing the performance of optical and electrical devices such as piezoelectric nanogenerators; however, well-defined Schottky contacts to the polar facets of the structures have yet to be explored. In this work, we demonstrate a process to fabricate metal−semiconductor−metal device structures from vertical arrays with Au contacts on the uppermost polar facets of the nanorods and show that the O-polar nanorods (∼0.44 eV) have a greater effective barrier height than the Zn-polar nanorods (∼0.37 eV). Oxygen plasma treatment is shown by cathodoluminescence spectroscopy to affect midgap defects associated with radiative emissions, which improves the Schottky contacts from weakly rectifying to strongly rectifying. Interestingly, the plasma treatment is shown to have a much greater effect in reducing the number of carriers in O-polar nanorods through quenching of the donor-type substitutional hydrogen on oxygen sites ($H_O$) when compared to the zinc-vacancy-related hydrogen defect complexes ($V_{Zn}$−$n$H) in Zn-polar nanorods that evolve to lower-coordinated complexes. The effect on $H_O$ in the O-polar nanorods coincides with a large reduction in the visible-range defects, producing a lower conductivity and creating the larger effective barrier heights. This combination can allow radiative losses and charge leakage to be controlled, enhancing devices such as dynamic photodetectors, strain sensors, and light-emitting diodes while showing that the O-polar nanorods can outperform Zn-polar nanorods in such applications.

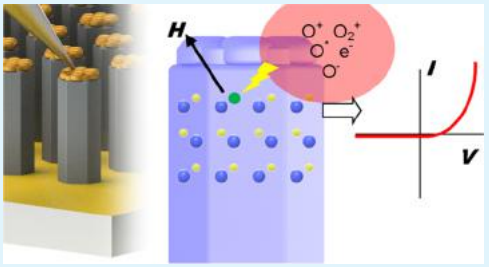


**KEYWORDS:** *ZnO, nanorods, polarity, Schottky contacts, electrical transport, cathodoluminescence, defects*

## 1. INTRODUCTION

ZnO belongs to the *6mm* point group with a wurtzite structure that leads to opposing polar facets that are predominantly Zn- or O-terminated.[1,2] On bulk ZnO crystals, the physical and chemical properties of these facets have been well-studied often to determine the surface band bending, electronic properties, and the resultant effect on electrical contacts to the polar surfaces.[3−6] Here, we extend this investigation to ZnO nanostructures to study the differences between electrical contacts fabricated on the uppermost but opposing polar facets of polarity-controlled vertical ZnO nanorods.[7] The ability to selectively pattern and control the morphology and spacing of the nanorods holds great promise to fabricate arrays with well-defined properties. Control of the crystal polarity provides an opportunity to determine the structure, electrical properties, and the all-important metal−semiconductor contacts that must be fabricated on the array tips to integrate them into nanotechnological devices. This is particularly critical in the applications of piezoelectricity including nanogenerators and pressure/strain sensors,[8,9] which benefit from the buildup of an electric field induced by piezoelectric polarization at a potential barrier.[10,11] In many of these devices, the formation of ZnO nanorods is achieved by chemical bath deposition on polycrystalline seed layers, which typically results in the creation of arrays with an uncontrolled/mixed polarity. In that case, a piezoelectric potential with opposite signs from a nanorod to nanorod can be generated and its magnitude further depends strongly on the Schottky contact properties on each individual nanorod.[10,11] This is also the case for vapor phase deposition techniques where reports show uncontrollable Zn-polarity when using a self-catalyzed approach, O-polarity has been observed when a metal catalyst is employed, and more importantly, the polarity is generally undefined.[12,13] This is a clear oversight when more often than not the polarity is unconsidered, even though it could be expected to drastically affect their electrical contacts and performance. Furthermore, extensive work on bulk ZnO crystals shows some variability in the behavior of Schottky contacts on the polar facets, while theoretical studies show a large difference in barrier height when comparing the O-polar and Zn-polar surfaces.[14,15] This suggests that there is an opportunity for selecting the contact and nanorod properties that have yet to be exploited on nanostructured crystals, and the issue remains largely unexplored in the case of ZnO nanorods despite its primary importance.

Received: December 30, 2019
Accepted: February 24, 2020
Published: February 24, 2020









https://dx.doi.org/10.1021/acsami.9b23260
*ACS Appl. Mater. Interfaces* 2020, 12, 13217−13228

Here, we investigate postgrowth metal contacts fabricated on the tips and to the array-base of individual polarity-controlled nanorods in the vertical periodic array configuration using a multiprobe scanning tunneling microscopy technique to reveal distinct differences between the two polarity types: Zn-polar [0001] and O-polar [000$\bar{1}$]. After an oxygen plasma treatment, it is revealed the O-polar orientated nanorods in general provide a greater effective barrier height (~0.44 eV) and more stable contacts than the Zn-polar orientated nanorods (~0.37 eV). Cathodoluminescence (CL) measurements performed on the same nanorods show that the incorporation of hydrogen in the lattice contributes to the n-type behavior, while there is a distinct difference of midgap defect states in the two nanorod types near the Au contacts. The oxygen plasma treatment is more effective at quenching visible-range defect states in the O-polar nanorods, increasing resistivity and providing higher-quality Schottky contacts than the Zn-polar nanorods. The work specifically highlights the potential superiority of O-polar ZnO nanorods, which justifies more intensive development to maximize their capabilities and effectively control the electrical contact properties with polarity-controlled growth. Demonstrated here is the ability to form metal−semiconductor−metal (MSM) structures on each nanorod in an array with one Schottky contact at the tip and a common Ohmic contact at the base. When these features are combined with the defined structural polarity, every nanorod of the array can contribute to the output of devices such as in energy-harvesting piezoelectric applications.

## 2. MATERIALS AND METHODS

**2.1. Nanorod Growth.** A 100 nm thick poly(methyl methacrylate) (PMMA) layer was spin-coated on the O- and Zn-polar ZnO single crystals (CrysTec) and then patterned identically by electron beam lithography (EBL). The hole circular diameter and period of 143 ± 8 and 1004 ± 6 nm were, respectively, used on the domain. The residual PMMA layer inside the holes was removed using oxygen plasma (OP) treatment with an Evactron radio frequency (RF) plasma cleaning system. Well-ordered vertical O- and Zn-polar ZnO nanorods were grown on the patterned O- and Zn-polar ZnO single crystals, respectively, using chemical bath deposition under identical conditions in the same experimental run. The solution was composed of a 30 mM equimolar concentration ratio of zinc nitrate hexahydrate [$Zn(NO_3)_2$, Sigma-Aldrich] and hexamethylenetetramine ($C_6H_{12}N_4$, Sigma-Aldrich), which were mixed in deionized water. The patterned O- and Zn-polar ZnO single crystals were placed face-down in separate beakers and heated to 90 °C for 3 h in a regular oven. The pH was set to the standard value of 5.5 at the growth temperature of 90 °C.

The O-polar nanorods typically have a lower growth rate than the Zn-polar nanorods under the same growth conditions, which led to the O-polar nanorods having a length of 4.41 $\mu$m, while the Zn-polar nanorods had a length of 5.59 $\mu$m.[16] The length of the nanorods for each sample was uniform across the patterned array area. The area of the top facets was estimated from the hexagonal cross-sectional shape that was measured from the scanning electron microscopy (SEM) images for each individual nanorod considered in the analysis of the electrical contact behavior and typically had a cross-sectional hexagonal side length of ~300 nm.

**2.2. Electrical Multiprobe Measurements.** We have previously reported a method using an Omicron LT nanoprobe multiprobe scanning tunneling microscope with in situ SEM capability, employing two tungsten probes annealed in situ[17] to measure Schottky and Ohmic contacts to the tips of as-grown vertical arrays of ZnO nanowires.[18,19] The method initially involves placing both probes on the sides of a single nanowire to test the contacts and ensure they are low-resistance and Ohmic in nature. In this work, this two-probe technique was initially employed on as-grown O- and Zn-polarity-controlled hydrothermally grown patterned ZnO nanorod arrays.[7] The generation of a piezoelectric potential that might occur during the deformation of the nanorods is expected to be minimal in the measurement process. The probes were approached with manual control of the piezomotors in nanometer steps to the Au contact using the tunneling feedback mechanism.[20] To reduce the surface contamination, the samples were treated with 20 s oxygen plasma treatment at ~$10^{-2}$ mbar and 50 W power before being transferred back to the UHV instrument after a short exposure to air. Subsequently, ~10 nm Au was evaporated onto the uppermost facets of the nanorods (samples were exposed to air before and after deposition).[21] Samples were loaded into the UHV instruments several days before ±2 V $I-V$ sweeps were taken for each contact. The presented data is an average of each of the individual measurements. The plasma processing and Au deposition were later repeated on previously masked portions of the same samples but with a further 6 min 75 W oxygen plasma treatment to improve the Schottky characteristics.

**2.3. CL Analysis.** 5 K CL measurements of single polarity-controlled nanorods covered with the Au contact on their tip were performed using an FEI Inspect F50 FESEM equipped with a liquid-helium-cooled stage. The CL signal was collected through a parabolic mirror and analyzed with a 550 mm focal length monochromator equipped with 600 grooves/mm diffraction grating. CL spectra were recorded with a thermoelectric-cooled silicon charge-coupled device (CCD) detector. The low acceleration voltage of 5 kV and small spot size (i.e., less than 10 nm) were used to create the CL signal at the center of the uppermost polar facet of every single nanorod close to the interface with the Au contact.

## 3. RESULTS

Electrical measurements with the multiprobe instrument were initially conducted on 31 O-polar and 31 Zn-polar vertical nanorods (Figure 1a) with Au contacts deposited on the upper polar facets after a short 20 s oxygen plasma treatment. To begin with, two probes were used, one on the Au contact top face and the other on the nanorod side near the base (Figure 1b). However, after several measurements, it was found that the $I-V$ characteristics were the same when using only one probe on the Au top contact (Figure 1c) and the sample stage as the low-potential probe, which was electrically connected to the large-area Au contact at the base of the nanorods, thus forming a MSM structure on each vertical nanorod. These initial measurements immediately displayed some difference between the two wire types with the Zn-polar nanorods showing greater electrical conductivity and weaker rectification (further experimental observations are given in the Supporting Information). In general, both of the nanorod types had poor rectification, which was judged by the lack of exponential current−voltage characteristics in the forward-bias and large reverse-bias current. Therefore, to improve the Au contacts further but without significant sputtering or depleting the O-polar and Zn-polar nanorods of charge carriers, they were treated with a further 6 min oxygen plasma treatment followed by Au contact deposition on a bare section of each array.

**3.1. Thermionic Emission in Au-Fabricated Contacts to Polarity-Controlled ZnO Nanorods.** A total of 28 O-polar and 24 Zn-polar nanorod−Au contacts treated with a 6 min oxygen plasma treatment were electrically measured, revealing a range of $I-V$ behavior (Figure 1d) between samples, and a large difference in rectification is immediately apparent. The Zn-polar and O-polar nanorods had lengths of 5.59 and 4.41 $\mu$m, respectively, and both had Au contacts with areas ranging between 1.5 × $10^{-9}$ and 3 × $10^{-9}$ $cm^2$, respectively, using identical growth conditions, owing to


https://dx.doi.org/10.1021/acsami.9b23260
ACS Appl. Mater. Interfaces 2020, 12, 13217−13228

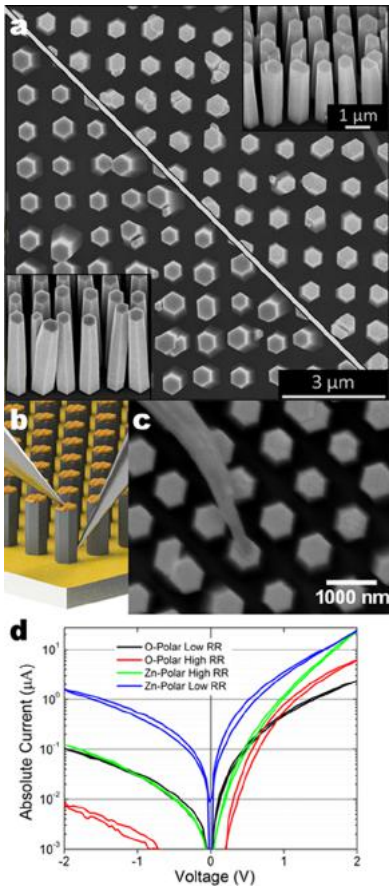


**Figure 1.** (a) Top−down and inset tilted SEM images of the O-polar nanorod array (upper) and the Zn-polar nanorod array (lower); (b) schematic diagram depicting the measurement configuration of vertical polar nanorods using two probes; (c) in situ SEM image of a single probe $I-V$ measurement of a Zn-polar nanorod with a fabricated Au contact on the (0001) top facet showing the tungsten probe and nanorod array; (d) $I-V$ graphs showing the greatest and least rectification ratio (RR) behavior for the O-polar and Zn-polar nanorods.

different surface reaction rate constants.[9] The Au contact covered the entire end facet and the semiconductor nanorod had one Ohmic contact at the base and one Schottky contact at the tip, allowing the $I-V$ data to be approximated in the low-forward-bias regime with standard thermionic emission theory.[22] This determined the effective potential barrier height ($\phi_e$) and ideality factor ($n$) of the Au−ZnO interface, and these were related to other properties such as the specific differential resistance,[22] rectification ratio (RR) at ±2 V, and estimated resistivity. Nanostructures typically present a large series resistance $R_s$, which must be taken into account, and this was measured from the high-forward-bias regime from each $I-V$ measurement. $R_s$ was calculated from the gradient $dV/dI$ near +2 V and was considered in the analytical term for thermionic emission theory and fit to the experimental data in the range $3kT/q < V < 0.35$ to determine the effective barrier height $\phi_e$ and ideality factor $n$ using

$$J = A^{**}T^2\, e^{(-q\phi_e/kT)}\, e^{q(V-IR_s)/nkT}$$

where $T$ is the temperature, $q$ is the electron charge, $k$ is the Boltzmann constant, and $A^{**}$ is the modified Richardson constant; however, it is acceptable to use the theoretical value $A^{**} = 32$ A/(cm$^2$ K$^2$). The Richardson constant takes into consideration the effective mass of electrons in the semiconductor $m^* = 0.27m_0$ for ZnO, where $m_0$ is the electron mass in vacuum.

To ensure that calculated values were accurate, they were compared to those given by Cheung and Cheung's method that provided similar values of $\phi_e$, $n$, and series resistance $R_s$.[23] In the case of non-negligible series resistance, the voltage becomes $V = V_\phi - IR_s$, where $V_\phi$ is the potential drop across the Schottky contact and $R_s$ is the series resistance attributed to the semiconductor and Ohmic contact. At low forward bias, the more conductive Zn-polar nanorod−Au contacts have $IR_s \ll 0.01$ V, less than the thermal voltage $kT/q$ at room temperature, giving a mostly negligible potential difference across the semiconductor in the voltage range used for calculating $\phi_e$. The series resistance is used here to assess the influence of the bulk properties when determining $\phi_e$, and the two properties are shown to be dependent in these nanorods. Fitting of analytical terms for thermionic field emission was attempted, but in the n-type doping range $\leq 10^{19}$ cm$^{-3}$, the depletion region is wide enough to make this component negligible at low forward bias.[24]

The average values of $\phi_e$ and $n$ for each nanorod are shown in Figure 2a, which reveals there is clearly a difference in the effective barrier height between the O-polar and Zn-polar nanorods; however, the ideality factor is large with a broad distribution in the O-polar nanorods. The maximum barrier heights measured on the O-polar nanosized contacts of ∼0.5

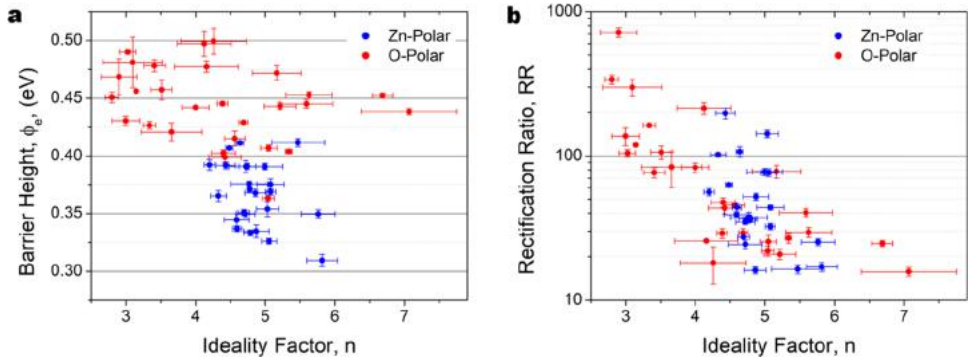


**Figure 2.** (a) Graph showing the relationship between ideality factor, $n$, and effective barrier potential height, $\phi_e$, for measured nanorods on the Zn-polar and O-polar samples after the oxygen plasma treatment. (b) Graph showing the rectification ratio of Zn-polar and O-polar nanorods with Au contacts plotted against the ideality factor.



https://dx.doi.org/10.1021/acsami.9b23260
ACS Appl. Mater. Interfaces 2020, 12, 13217−13228

eV compare favorably with the typical barrier heights of ∼0.6 eV that are measured on high-quality, large-scale Au contacts fabricated on clean ZnO surfaces in vacuum.[25] Au contacts on plasma-treated bulk $(000\bar{1})$ ZnO have measured values of 0.48 and 0.43 eV, depending on whether the ZnO was deemed to have low or high defect concentrations, respectively.[4] An approximate linear increase of $\phi_e$ with decreasing $n$ is apparent for the majority of the O- and Zn-polar nanorods, which theoretically is a symptom of inhomogeneous contacts, but this can also indicate a change in carrier concentration.[26,27] It should be noted that for ideal thermionic emission the current is determined by the barrier height, but for materials of varying carrier concentrations, $\phi_e$ can vary widely. Therefore, it is important to differentiate between bulk variations in the samples and determine whether the different polar orientations have an appreciable effect on $\phi_e$.

*3.1.1. Estimating the Influence of Bulk Properties on the Au Contacts.* To investigate the bulk properties of nanorods, their electrical resistivity was estimated from the voltage range greater than the flat-band condition in the $I-V$ measurements at high forward bias (+2 V) when electron flow is unperturbed by the potential barrier. The results are summarized in Table 1

**Table 1. Average Values Calculated from the Electrical Measurements of Au−Nanorod Contacts on the Two Polarity-Controlled Arrays**

| polarity | $\phi_e$ (eV) | $n$ | RR | est. resistivity (Ω cm) | $R_c$, $dV/dJ_{V=0}$ (Ω cm$^2$) | $J_{rev}$ at −2 V (A/cm$^2$) |
|---|---|---|---|---|---|---|
| O-polar | 0.44 | 4.3 | 106 | 13.6 | 1.18 | 6.2 |
| Zn-polar | 0.37 | 4.9 | 56 | 0.6 | 0.08 | 123.2 |

and shown graphically in Figure S1a, which depicts $\phi_e$ increasing predictably as the resistivity increases, which can be directly related to decreasing carrier concentration in the ZnO nanorods. The estimated nanorod resistivity of the two samples shows average values of 0.6 and 13.6 Ω cm for the Zn-polar and O-polar nanorods, respectively, with more than 1 order of magnitude difference between samples.

The average estimated resistivity values of the nanorods are nearly 2 orders of magnitude greater than the four-probe resistivity of as-grown samples and significantly different between the two samples. Nanorods grown by the same method with identical conditions have previously been measured in the four-probe configuration, revealing average resistivities in the Zn-polar and O-polar orientation of $1.1 \times 10^{-2}$ and $9.8 \times 10^{-2}$ Ω cm, respectively.[28] By assuming an electron mobility ranging from 50 to 100 cm$^2$/(V s), these values correspond to respective carrier concentration ranges of $5.4 \times 10^{18}-1.1 \times 10^{19}$ and $6.4 \times 10^{17}-1.3 \times 10^{18}$ cm$^{-3}$, which was mainly attributed to hydrogen-related defects incorporated during growth, namely, substitutional hydrogen on an oxygen lattice site ($H_O$), multiple O−H bonds in a zinc vacancy ($V_{Zn}-nH$), and interstitial hydrogen in bond-centered sites ($H_{BC}$). The previous analysis showed that the dominant donors differed between the polarity types where the O-polar nanorods had a significant concentration of $H_O$, while ($V_{Zn}-nH$) was predominantly revealed in Zn-polar nanorods, along with a high density of $H_{BC}$ in both cases.

This large change in the resistivity of the nanorods measured here is a result of the oxygen plasma treatment. Initially, in the first round of measurements, the samples were treated with a 20 s plasma exposure, giving average estimated resistivities of 0.11 and 0.33 Ω cm for the Zn- and O-polar nanorods, respectively. The relatively small initial difference in resistivity between the samples appears to have been inherited from the growth process, but this difference in donor defects is likely to have had a large influence on the interactions with the full oxygen plasma treatment. The 6 min plasma treatment had a much greater effect on the O-polar nanorods, substantially increasing the resistivity by a factor of 40 compared with a lesser effect on the Zn-polar nanorods, which also coincides with a considerable effect increasing RR and $\phi_e$ for both samples.

*3.1.2. Interfacial Layer.* The samples have a similar average ideality factor, but the Zn-polar nanorods have a much smaller range of $n$, while a significant number of O-polar nanorods do not fit the linear relationship with $\phi_e$ (Figure 2a). This difference in the samples is shown again by plotting the rectification ratio against the ideality factor, shown in Figure 2b.

RR is useful as a figure of merit for rectifying contacts when exponential current−voltage relationships are not appropriate, and it is defined here as

$$\mathrm{RR} = \frac{\text{current at } +2V}{-\text{current at } -2V}$$

Figure 2b reveals RR rapidly increasing with decreasing ideality factor for the O-polar nanorods, while the Zn-polar nanorods are grouped together with a wide range of RR. The data for the O-polar nanorods shows that there is a relationship between the low-bias ($n$) fit to thermionic emission theory and the high-bias regime (RR), while this is less obvious for the Zn-polar nanorod−Au contacts. This suggests that the conduction mechanisms that can contribute to weak rectification, reverse-bias leakage, and low RR also govern nonideal behavior at low forward bias in the O-polar nanorods, namely, tunneling, defect-assisted tunneling/hopping, and interfacial phenomena such as barrier inhomogeneity and interfacial layers.

A range in rectifying behavior is evident across both samples but with O-polar nanorods on the whole being greater rectifiers with larger RR and $\phi_e$ (Table 1 shows average values for each sample). Oxygen plasma treatments on bulk ZnO surfaces for short periods (e.g., 5 min) are thought to have an effect limited to the surface and near-surface, and as such, the bulk carrier concentration is largely unaffected.[29,30] However, for small structures, the oxygen plasma must be assumed to react strongly with the surface and also penetrate the entire bulk of the nanorod, affecting the carrier concentration. Tunneling is a major cause of nonideal thermionic behavior, and it is directly related to donor density. Therefore, we might propose in Figure 2b that nanorods with a greater conductivity would have increased reverse-bias tunneling, giving a low RR and high $n$. However, this is not entirely the case. Rather, we find a general trend of both reverse-bias current decreasing and high-forward-bias current increasing with decreasing $n$ and increasing RR. This is depicted in Figure S1b, showing that both samples have an increasing trend of RR with decreasing resistivity but with little correlation between samples. This indicates the presence of an interfacial layer that with increasing thickness reduces the current in forward bias and increases the current in reverse bias, increasing the measured resistance, reducing RR, and increasing $n$. It is unclear whether this is due to an oxygen-rich surface layer created by the


https://dx.doi.org/10.1021/acsami.9b23260
ACS Appl. Mater. Interfaces 2020, 12, 13217−13228

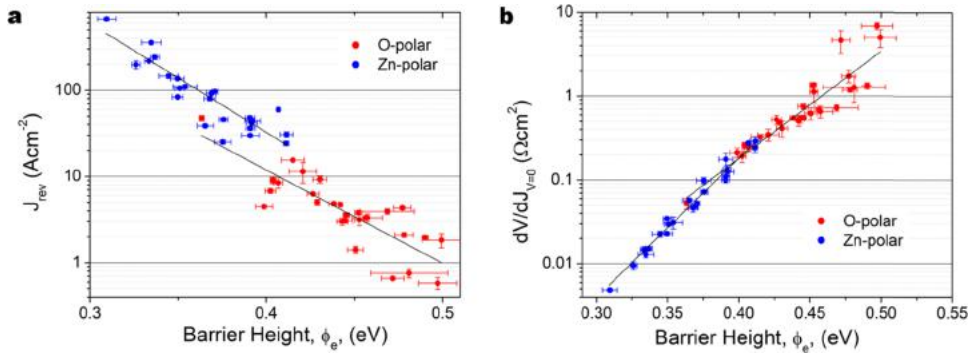


**Figure 3.** (a) Graph showing the average current density for each nanorod at −2 V reverse bias plotted against $\phi_e$ and showing exponential functions fitted to each data set. (b) Graph showing the relationship between the specific differential resistance for each of the O-polar and Zn-polar nanowires and the exponential fit to each data set.

plasma, a range in oxygen vacancy ($V_O$) density near the interface creating a region of positive space charge that can lead to nonideal behavior and low RR (Figure 2b),[31] some remaining surface contamination, or an electrostatic effect that depends on the polar terminations and structure (also linked to point defects). Furthermore, it can be seen in the experimental graphs in Figure 1d, particularly for the O-polar nanorod (red), that splitting of the $I-V$ trace in reverse bias occurs when the current is relatively small. This splitting is a capacitance effect attributed to charging and discharging of interface and midgap states created by defects,[32] which is not appreciable for the more conductive nanorods measured here, which have current density values well above those measured on much larger contacts to bulk single crystals.[14,27]

In reality, knowing that the carrier concentration of as-grown nanorods within each sample varied by a factor of 2, then variations in both carrier concentration and interfacial layer thickness can explain Figure 2a,b. It is possible to identify the nanorods that are least affected by an interfacial layer: they have a high RR, low estimated resistivity, and a low ideality factor, although this is sensitive to transport mechanisms present at low bias. Additionally, we can then state that the most reliable estimates of resistivity for nanorods least affected by an interfacial layer from within each sample are ∼0.1 Ω cm for the Zn-polar nanorods and ∼3 Ω cm for O-polar nanorods, at least a decade higher than the average four-probe resistivity for their as-grown counterpart. The various estimates all show that the greatest change to the bulk resistivity occurred to the O-polar nanorods after the oxygen plasma treatment.

RR appears to be a better indicator of the actual interface quality because of the dependence of $\phi_e$ on carrier concentration. The lack of correlation of RR with estimated resistivity across the two samples further shows that the bulk conductivity is not the only factor driving RR for each contact. The measurements show that after the oxygen plasma treatment the two samples have different bulk properties, but both experience a range of interfacial phenomena as a result of variable insulating layers.

*3.1.3. Evidence for Defects and Capacitance.* Thermionic emission theory predicts that the reverse-bias current[22] should saturate at $J_0 = A^{**}T^2\, e^{(-q\phi/kT)}$, and Figure 3a shows that the reverse-bias current holds an exponential relationship with $\phi_e$, which follows $J_{rev} \sim e^{-28.06\phi_e}$ for the Zn-polar nanorods, while the O-polar nanorod data fits $J_{rev} \sim e^{-24.12\phi_e}$. The large error in the thermal voltage value for both data sets is a result of the high reverse bias (−2 V) used to calculate $J_{rev}$ that is predominantly tunneling through the thin depletion region, which is affected by variations in carrier concentration and the barrier height. However, the O-polar nanorod data in Figure 3a shows a greater divergence from thermionic emission theory, particularly when $\phi_e \rightarrow 0.5$ eV, and these contacts have a large range in $n$ and RR. There is increased scatter in the O-polar nanorod data at large $\phi_e$ because the reverse-bias current is small, unmasking the effects of interfacial layers/defects and defect states in the depletion region that vary between contacts and influence defect-assisted transport, tunneling, and capacitance. In this selection of contacts, those with the smallest $J_{rev}$ have high RR and low $n$.

A term that is often used for analyzing nanosized Schottky contacts is the specific differential resistance ($R_c$) at zero bias, which has been employed to identify increased conductivity due to the presence of dopant atoms and also for identifying recombination current in nanowires.[22,33,34]

$R_c$ ($\Omega$ cm$^2$) is calculated from current−voltage behavior at $V$ = 0 and is defined as

$$R_c = \left\{\frac{\partial V}{\partial J}\right\}_{V=0}$$

where $J$ is the current density calculated using the measured Au contact area from the SEM images of each individual nanorod.[35] Figure 3b shows a graph of $R_c$ in relation to $\phi_e$. Typically, a range of $R_c$ of 3 orders of magnitude can be expected for variability in nanorod resistivity of 2−3 orders of magnitude, consistent with the measurements here.[36]

For relatively lightly doped materials with $N_d < 10^{18}$ cm$^{-3}$, it was shown by Yu that the specific differential resistance $dV/dJ_{V=0}$ when tunneling is negligible goes like $e^{(q\phi/kT)}$ and is independent of doping.[37] That is in the case of pure thermionic emission, and since the nanorods have the lowest resistivity of 0.05 Ω cm, the relationship between $R_c$ and $\phi_e$ should follow this form. Fitting exponential forms to the data in Figure 3b shows a good fit to the Zn-polar data with $R_c \sim e^{39.06\phi_e}$, while the O-polar data has a much weaker correlation with $R_c \sim e^{29.19\phi_e}$. The scatter that was seen in Figure 3a is also evident here in the deviation from thermionic emission theory of the O-polar nanorods at large $\phi_e$. Furthermore, nanorods that deviate from the behavior of decreasing ideality factor with increasing barrier height are seen in Figure 2a, and they have a large $n$ but relatively large $\phi_e$. However, many of the nanorods that deviate from the thermionic emission fit in Figure 3b have $n < 4$, large RR, and $\phi_e$ but with $R_c < 2$ Ω cm$^2$, lower than


https://dx.doi.org/10.1021/acsami.9b23260
ACS Appl. Mater. Interfaces 2020, 12, 13217−13228

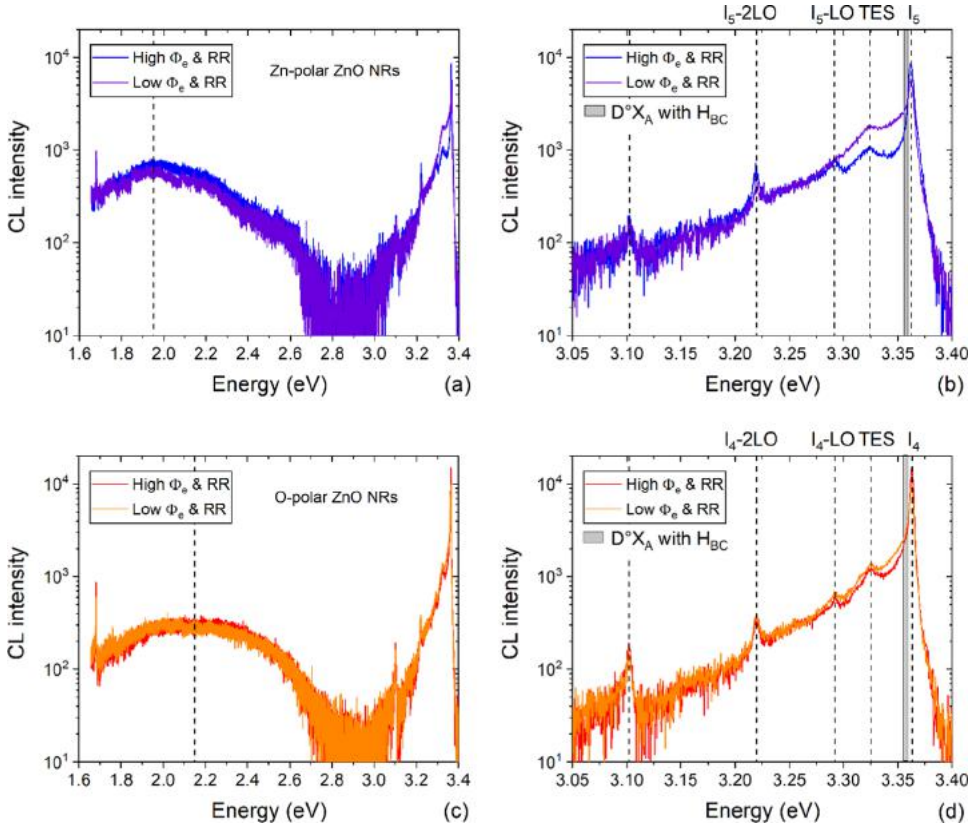


**Figure 4.** (a) Representative CL spectra of Zn-polar nanorods with (b) special emphasis on the NBE emission region in the case of high $\phi_e$ and RR as well as low $\phi_e$ and RR. (c) Representative CL spectra of O-polar nanorods with (d) special emphasis on the NBE emission region in the case of high $\phi_e$ and RR as well as low $\phi_e$ and RR. The CL spectra were recorded near the Au contact interface on the uppermost polar facets, and the same conditions were used for each polarity, except the acquisition time that was 60 and 10 s for Zn- and O-polar nanorods, respectively.

expected from theory. Deviations of $R_c$ can be a result of a capacitance effect from the trapping and release of charge carriers, while transport mechanisms that occur near zero bias include defect-assisted tunneling. The capacitance effect is evident in the splitting of the $I-V$ trace (Figure 1d), indicating the release of charges at low bias on the reverse $I-V$ sweep (+2 to −2 V) of a triangulation from zero bias, and the more the released charge, the lower the measured $R_c$. However, these effects are not apparent in the Zn-polar nanorod data due to the significantly higher current at low bias. Barrier inhomogeneity is contained within the measured effective barrier height and ideality factor, while an insulating interfacial layer acts to increase $R_c$ unless the layer introduces defects with a capacitance effect. Instead, the current in the low-bias regime when the contact barrier is large is also affected by erroneous influences, such as defect-assisted tunneling and the trapping and release of charges at or near the interface.

The data has shown that a significant difference exists between the O-polar and Zn-polar nanorods and the subsequent Schottky contacts that are formed. Plasma-treated O-polar nanorods are significantly less conductive and the Au contacts form larger effective potential barriers, while variable interfacial layers and defects play a prominent role in determining the contact properties. The greater conductivity of the Zn-polar nanorods results in lower effective potential barriers that are also affected by interfacial layers, while the larger current masks the influence of defects on the transport mechanisms. An inherent difference is known to exist between the donor defects in the O-polar and Zn-polar as-grown nanorods,[28] but the interaction of these defects with the oxygen plasma is unclear. The plasma treatment creates oxygen ions that react with the surface layers and growth residues, forming oxygen reactive species with carbon molecules, water, and adsorbed oxygen, while more energetic ions penetrate the subsurface of the ZnO.[38] Prolonged oxygen plasma treatments are thought to increase the surface depletion region while affecting bulk defects of single-crystal ZnO such as interstitial and substitutional donors, increasing the resistivity.[38] Furthermore, the oxygen ions are known to reduce donor OH surface groups associated with surface conduction effects normally seen on bulk single-crystal ZnO; introduce $O_2^-$, further reducing carriers near the surface; and eliminate oxygen vacancies even within the subsurface region, which can all affect the barrier and transport mechanisms.[29,38,39] ZnO nanorods grown by chemical bath deposition exhibit a high density of surface defect states, and oxygen ions may cure most of them, affecting in turn the depletion layer with a reduction in carrier concentration and changes to the surface potential. To reach a deeper understanding of the bulk and near-surface defects, several nanorods with Au contacts used for the electrical measurements and from the same samples were analyzed with CL spectroscopy.

**3.2. Cathodoluminescence of Polar ZnO Nanorods with Au Contacts.** The oxygen-plasma-treated Zn- and O-polar nanorods with Au contacts were analyzed by CL measurements at 5 K to probe the radiative emissions of ZnO near the contact interface. CL has been used in numerous works to identify donors, defects, and metal-induced gap states


https://dx.doi.org/10.1021/acsami.9b23260
ACS Appl. Mater. Interfaces 2020, 12, 13217−13228

(MIGSs) in Schottky contacts to nanostructured and single-crystal ZnO.[4,40−42] CL spectroscopy was performed on the same nanorods that were measured electrically with a small spot size and the beam parallel to the vertical nanorods and focused on the Au contact with an energy of 5 keV. The expected probing depth concentrating more than 75% of the energy was ∼20 nm below the Au surface and approximately 10 nm below the Au−ZnO interface and spreading further into the bulk.[40]

CL measurements were collected for 11 O-polar and 14 Zn-polar nanorods after oxygen plasma treatment and with Au contacts, and representative spectra are shown in Figure 4, exhibiting a strong difference in their intensity. The Zn-polar nanorods treated with the oxygen plasma have a lower CL intensity than all of the O-polar nanorods treated with the oxygen plasma, and both have much lower intensities than their as-grown counterparts. Furthermore, the intensity is similar for both samples when analyzing the Au−ZnO region on the single-crystal substrates between the nanorods; thus, the effect is unique to the nanorods and excludes any significant difference in Au thickness. This indicates the formation of nonradiative recombination centers in Zn-polar nanorods, following the oxygen plasma and Au contact deposition.[43] As regards to the nature of radiative transitions involved, the CL spectra of O- and Zn-polar nanorods treated with the oxygen plasma are, however, to a large extent similar to those of the bare as-grown nanorods in the most dominant near-band-edge- (NBE) emission region, but a couple of striking differences occur in the vicinity of the NBE region and in the visible bands. The CL spectra show the dominant NBE emission at around 3.36 eV and additional emissions at 3.324, 3.292, 3.220, and 3.102 eV. One can notice that, even while performing the analysis through the Au contact, the NBE emission is dominated by radiative transitions involving neutral donor-bound A-excitons, systematically the $I_4$ line (i.e., $H_O$) at 3.3627 eV[44] in the case of O-polar nanorods and the $I_5$ line [i.e., ($V_{Zn}$−$n$H) defect complex] at 3.3616 eV[45] in the case of Zn-polar nanorods. This is in agreement with previous analysis of similar nanomaterials and provides the ability to non-destructively assess the polarity of each measured individual ZnO nanorod grown in this way.[28] For both polarities, a broad shoulder at around 3.358 eV additionally occurs, involving neutral donor-bound A-excitons related to $H_{BC}$.[44] The two related lines at around 3.292 and 3.220 eV correspond to the first and second longitudinal optical (LO) phonon replicas of that dominant NBE emission, respectively, each of them being separated by a phonon energy of 72 meV in ZnO.[46] The line located at around 3.324 eV occurs in the CL spectra of O-polar and Zn-polar nanorods with a varying intensity and is usually attributed to a two-electron satellite (TES) line.[46] However, this line was not present in that energy position on bare as-grown O-polar and Zn-polar nanorods exhibiting a shift of 8 meV to lower energy. TES transitions are sensitive to sample processing and related to donor-bound excitons and carrier concentration.[46] Similarly, the line at 3.102 eV is also much more prominent. It is therefore possible that both lines could be associated with the oxygen plasma treatment and Au contact, such as a mild sputtering effect creating surface states, displaced lattice atoms or hydrogen, or reactions of the oxygen ions or Au with the lattice and surface species.

The intensity ratio $I_R = I(\mathrm{NBE})/I(\mathrm{Vis})$ of the NBE emission over the visible band drastically decreases for both polarities following the oxygen plasma treatment and Au contact deposition, and $I_R$ is noticeably larger for the O-polar nanorods. $I_R$ has average values of 26 and 10 for the O-polar and Zn-polar nanorods, respectively. In contrast, this intensity ratio for both polarities is quite similar in as-grown nanorods and even slightly larger for Zn-polar nanorods, even though the carrier concentration in their bulk differs.[28] Accordingly, in the measurements performed here, the visible band is more pronounced for the Zn-polar nanorods when compared to the O-polar nanorods and we can thus expect a higher density of related defects. There is also a clear difference in the contributions involved in the visible band from the CL spectra with the broad peak centered over ∼1.95 eV in the Zn-polar nanorods and at ∼2.15 eV in the O-polar nanorods. This broad peak can be split into several components identified as the green (i.e., 2.4 eV), yellow (2.2. eV), and red-orange (i.e., 1.8 eV) visible bands in the literature, but their assignment to native point defects is still highly debated.[47] However, one can expect, from the most recent theoretical calculations,[48,49] that the red-orange visible band at around 1.9 eV is attributed to zinc-vacancy-related defect complexes, with some of them being ($V_{Zn}$−H) and ($V_{Zn}$−2H) defect complexes or zinc interstitials.[43] The green luminescence, previously attributed to a large extent to zinc- or oxygen-vacancy-related defects,[50,51] may also be correlated with zinc atom dangling bonds.[48]

## 4. DISCUSSION

Correlating the CL analysis to the $I$−$V$ data of both samples would suggest that the visible-range defects are directly related to the difference in the barrier height and electrical resistivity of the two samples. In particular, the increase in the electrical resistivity by prolonging the oxygen plasma treatment can to some extent be explained by the CL spectra in Figure 4. The oxygen plasma treatment provides high-energy oxygen ions and hence oxygen-rich conditions that can fill the vacant oxygen sites on the surface and in the bulk as previously occupied by the hydrogen, decreasing in turn the density of $H_O$ and thus the intensity of the $I_4$ line in O-polar nanorods, as shown by the experimental data (Figure 4c,d) and compared to as-grown nanorods. Additionally, these conditions are favorable to massively form zinc vacancies with a very low formation energy in that range of oxygen chemical potential and Fermi level energy,[48] which somehow balance the number of interstitial hydrogen (i.e., $H_{BC}$).[52,53] This can lead to the formation of ($V_{Zn}$−$n$H) defect complexes with a decreasing $n$ [i.e., preferentially ($V_{Zn}$−H) and ($V_{Zn}$−2H) defect complexes], thus decreasing in turn the density of ($V_{Zn}$−3H) donor defect complexes and hence the intensity of the $I_5$ line in Zn-polar nanorods. Consequently, the red-orange visible band recently attributed to these zinc-vacancy-related defect complexes is much more pronounced following the oxygen plasma treatment and Au contact deposition, particularly in the Zn-polar nanorods. This present statement accounts for the decrease in the intensity ratio of the NBE emission over the visible band following the oxygen plasma treatment and Au contact deposition. Overall, in the case of Zn-polar nanorods, the majority of ($V_{Zn}$−3H) defect complexes acting as donors are progressively replaced by the ($V_{Zn}$−H) defect complexes acting as acceptors and by the neutral ($V_{Zn}$−2H) defect complexes following the oxygen plasma treatment. In the case of O-polar nanorods, the majority of $H_O$ defects acting as shallow donors are also annihilated to some extent by the oxygen plasma treatment. For both polarities, the density of $H_{BC}$ defects acting as shallow donors is further expected to be


https://dx.doi.org/10.1021/acsami.9b23260
ACS Appl. Mater. Interfaces 2020, 12, 13217−13228

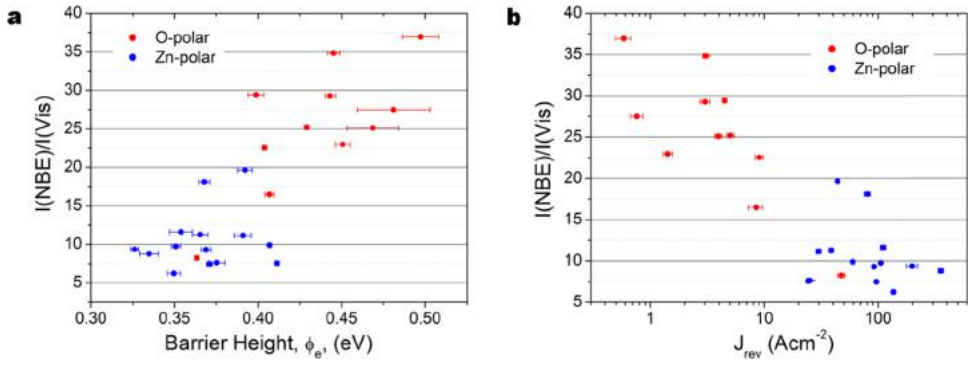


**Figure 5.** Graphs comparing the CL data for both samples with properties of the Au−ZnO contacts. (a) Intensity ratio of the NBE emission and visible band ($I_R$) against barrier height ($\phi_e$); (b) intensity ratio of the NBE emission and visible band ($I_R$) against the current density at −2 V ($J_{rev}$).

reduced as well, possibly forming highly mobile $H_2$ molecules diffusing out from the sample.[54] Furthermore, the much reduced radiative intensity of the Zn-polar nanorods suggests the formation of nonradiative recombination centers, while the oxygen plasma acts more selectively on donor defects in the O-polar nanorods. This can also explain the smaller change in the resistivity of the Zn-polar nanorods after the oxygen plasma treatment. All of these related effects result in the decreased carrier concentration and thus in the increased resistivity shown in the $I-V$ measurements following the oxygen plasma treatment and Au contact deposition.

Experimentally, Kennedy et al. have recently shown for individual ZnO nanowires that emissions between 2.10 and 2.97 eV (yellow to blue) are predominantly associated with surface defects and those at lower energy (red) deeper within the band gap originate in the bulk.[55] Using this knowledge, emissions from the Zn-polar nanorods show a greater weighting of bulklike defects where zinc-vacancy-related defects exist throughout the lattice, but their compensating role is reduced through hydrogenation, which was previously shown to contribute to the difference in the O- and Zn-polar nanorod resistivity.[28] The ($V_{Zn}-nH$) defect complexes are thought to be formed during growth, and they are unlikely to dissociate.[48] Therefore, it appears that the O-polar nanorods that have carriers originally contributed from $H_O$, may have bulk related donor defects that are more easily annihilated by the oxygen plasma. The O-polar nanorod defects are weighted toward the green luminescence after the plasma treatment, but the relative intensity in this energy range is comparable to that of the Zn-polar nanorods. We cannot discount that the larger O-polar nanorod $I_R$ could be due to quenching of red-orange bulk defects by the oxygen plasma in the O-polar nanorods or the more favorable creation of nonradiative recombination centers in the Zn-polar nanorods.[43,48] However, such large red luminescence intensity was not present in the as-grown nanorods. As such, the Zn-polar nanorod emissions exhibit a proportionally greater contribution from defects throughout the red to the blue visible range but with a lower radiative intensity. Nonradiative defects are associated with $V_{Zn}$ and $V_O$ deeper within the band gap where nonradiative recombination is more likely with such transitions often going undetected.[48] Both samples exhibit a much lower $I_R$ than as-grown nanorods, which may to some extent be due to MIGSs, which have been shown to reduce $I_R$, but MIGSs also have similar characteristics to native defects in CL spectra with the visible bands appearing similar before and after metal deposition.[4]

Considering the penetration depth of the electron beam, the recorded emissions can be considered to be near the interface and within the contact depletion region, subsequently affecting the potential barrier, barrier inhomogeneity, and transport mechanisms. Figure 4 shows the CL spectra of nanorods in both samples, comparing those with contacts with relatively high $\phi_e$ and RR to those with low $\phi_e$ and RR. In the NBE region, there is a decrease in the intensity of the TES line and the shoulder related to $H_{BC}$ for higher $\phi_e$ and RR in the Zn-polar nanorods, while this is less pronounced in the O-polar nanorods. This suggests that there is a variable effect of the oxygen plasma treatment and Au contact on the neutral donor-bound excitons that generate the TES line and $D^0X_A$ shoulder and to some extent influence the interface and contact transport properties. It is possible that, due to the variable interfacial layer, the effect on the TES line is a result of metal-induced interactions with the electronic states near the interface. Also, of note is that the visible defect bands are very similar for both large $\phi_e$ and small $\phi_e$. This indicates that the range of $\phi_e$ in each sample is related to the nature and variation of the donor defects near the interface, as indicated by variations in the NBE region that can create barrier inhomogeneity and influence tunneling.

Figure 5a directly correlates the electrical measurements to the CL data. It is immediately apparent that the O-polar nanorods show a trend of increasing $I_R$ with increasing $\phi_e$, while the Zn-polar nanorods show only small changes. The same trend is also seen with $I_R$ increasing with estimated resistivity and specific differential resistance. The lower concentration of visible-range defects in the O-polar nanorods coincides with the larger effective barrier height and greater resistance. This is consistent with other reports, albeit previously found when oxidized metals on the O-polar facet of bulk crystals had higher concentrations of visible band defects ($V_{Zn}$, $V_O$) and higher carrier concentrations, reducing the height of Schottky barriers when compared with the Zn-polar facet, depending on the growth method.[41] No trend in the CL data with RR was found, suggesting that the defects that were probed with CL affect transport mechanisms at low forward bias and the calculation of $\phi_e$ but are not the determinant of RR. This is further evidence that RR is largely affected by the interface quality such as interfacial layers and the associated transport mechanisms that was exhibited by the lack of correlation between RR and $\phi_e$ in the electrical measurement data. The detrimental effect of visible-range defects on the Schottky contact function is displayed in Figure 5b, which shows $J_{rev}$ increasing with the intensity of the visible-


https://dx.doi.org/10.1021/acsami.9b23260
ACS Appl. Mater. Interfaces 2020, 12, 13217−13228

range emissions (and decreasing $I_R$), which also coincides with an increase in conductivity and decrease in $R_c$. The defects that lead to a greater carrier concentration enhance tunneling in reverse bias and degrade the contact function, while subsurface defects may also contribute to the transport at low forward bias, decreasing the measured $\phi_e$, especially for the Zn-polar contacts. The growth rate of the O-polar nanorods is lower, and the incorporated defects result in a greater range of as-grown resistivity, which even after oxygen plasma treatment may contribute to the greater range of $I_R$ and $n$ in the O-polar nanorods.[16,28] The Zn-polar nanorods show a small range of $I_R$, which corresponds to a small range and high values of ideality factor $n$. This adds to the premise that defects in general contribute to nonideal thermionic emission. The ideality factor will is also by defect-assisted transport and charge trapping, which has been shown to be present with the analysis of $J_{rev}$ and $R_c$. However, when $n$ is compared to $J_{rev}$, $R_c$, estimated resistivity, $\phi_e$, and RR, the only correlation is with $\phi_e$ and RR (Figure 2). An insulating layer reduces current at low forward bias in the linear region of the $ln\ J-V$ data where $n$ is measured and a lower current for a given barrier height gives a larger $n$. The higher-quality O-polar nanocontacts, with low $n$, result from fewer donors/defects when compared to the Zn-polar nanorods, evidenced by greater $I_R$ and higher resistivity, which are a product of a more effective plasma treatment. However, $I_R$ is not a good indicator for the contacts that have a relatively large $\phi_e$ and relatively large $n$, suggesting the radiative defects do not play a major role in the nonideal transport of these contacts but may instead be attributed to the presence of an interfacial layer because they have low RR. This also points to the lack of any overriding relationship of MIGS with the interfacial layer and by association with the contact function. Therefore, in general, the greater $\phi_e$ measured for O-polar nanorods is a direct result of fewer lattice/surface defects and carriers creating less conductive nanorods that were affected by the oxygen plasma to a greater extent than the Zn-polar nanorods.

Defect states within the band gap can influence the contact potential barrier, depletion region, carrier concentration, and transport mechanisms, with $V_O$ particularly known to influence the barrier height and ideality factor.[31] Additionally, metal-induced energy levels within the band gap may be specific to the O-polar or Zn-polar facets, with varying point defects associated with each surface. Simulations of metal interfaces and polar facets have shown a range of MIGSs within the band gap that are much more pronounced on Zn-terminated facets.[15] These MIGSs are well screened from the bulk ZnO and really only affect the interface density of states, and they are expected to be less dominant in ZnO when the density of states due to crystallographic point defects may be higher than that from MIGS.[15,31] This would suggest, and in agreement with the CL spectra and $I-V$ measurements, that major variations in NBE and defect emissions found between each of the polarities are not due to variations in MIGS but primarily variations in subsurface and bulk defects. The conducting states arising from the junction of the Au and ZnO are theoretically predicted to occur very close to the interface and emerge within the first ZnO layer.[15,56] However, in reality, the Au junction in these nanorods may not be perfectly abrupt in a theoretical sense and so a variable influence on the electrical properties is a possibility. Theoretically, the anionic surface can give greater barrier heights on polar surfaces, and first-principles calculations by D'Amico et al. predict the O-polar interfaces to have a larger 0.7 eV barrier height with Au than the 0.3 eV at the Zn-polar interface.[15,57] The metal contacts formed here on as-grown polar facets were treated only with oxygen plasma and as such can be expected to have a surface structure close to that of free and reconstructed polar ZnO with a mix of terminating O or Zn atoms and not epitaxial with the Au. Furthermore, numerous techniques have identified a range of deep and shallow traps in ZnO that are inherent from the growth process or they can be introduced by plasma exposure, although not all of these are electrically active at 300 K.[58] Predominantly, carrier traps are assigned to various defects such as $V_O$, $V_{Zn}$, Zn interstitials, and divacancies of ZnO, with $V_O$ being the most common that can act as a trap for both electrons and holes.[59,60] Electrically active defects located in the depletion region may appear in the transport measurements identified as the splitting of the $I-V$ trace seen in some of the contacts (Figure 1d) particularly in reverse bias. These defects may occur throughout the band gap, coinciding with conducting or trapping states as the negative bias is swept. Traps can also occur at the interface and are expected to be distinct not only for each polar facet but also from a nanorod to nanorod because of structural variations that may have emulated an interfacial layer here as a variable layer of charge near the polar facets.[31,61] This complexity in determining the nature of the interface next to bulk and subsurface contributions makes it problematic to identify any definite difference in the Zn-polar and O-polar contact interfaces studied here. However, the ability to modulate the free carriers and effective barrier height through simple treatments shown here can enhance applications such as piezoelectric devices, reducing piezopotential screening and controlling charge leakage with tunable Schottky barriers.[10,11] The next step is to tailor the MSM array devices for specific applications, with piezoelectric energy generation being a prime example, while the contact interfaces could be enhanced further with improved cleaning of the polar facets, passivation, or homogenizing electrostatic phenomena, such as with self-assembled molecules (SAMs), and further reductions of bulk defects that lead to midgap states and carrier traps.

## 5. CONCLUSIONS

It has been shown that polarity-controlled nanorods can be modified to produce Schottky contacts on the tips of vertically standing nanorods in the patterned array configuration, creating a metal−semiconductor−metal device structure and making their integration into nanotechnological devices possible. Analysis of the electrical transport behavior in combination with cathodoluminescence spectroscopy has shown that defects related to the polar orientation of the nanorods incorporated during growth can determine the Schottky contact behavior. Quenching of surface and lattice defects with oxygen plasma reduces the conductivity and increases the potential barrier height. Interestingly, the plasma treatment was shown to have a much greater effect in reducing the donor-type substitutional hydrogen on oxygen sites ($H_o$) than zinc-vacancy-related hydrogen defect complexes ($V_{Zn}-nH$), which coincided with a large reduction in the visible-range defects in the O-polar nanorods. It was shown that the oxygen plasma was more efficient at reducing the visible-range emissions in O-polar nanorods when compared to Zn-polar nanorods reducing the carrier concentration and creating larger Schottky barriers. O-polar nanorods are largely unexplored for many applications but have proved here to be


https://dx.doi.org/10.1021/acsami.9b23260
ACS Appl. Mater. Interfaces 2020, 12, 13217−13228

superior to the Zn-polar nanorods that are predominantly exploited in nanodevices. This finding warrants further investigation to establish a full understanding of nanocrystals with differing polarities. The results show a strategy for creating high-quality Schottky contacts that can be used for enhancing nanotechnological devices such as piezoelectric nanogenerators.

## ■ ASSOCIATED CONTENT

### Supporting Information

The Supporting Information is available free of charge at https://pubs.acs.org/doi/10.1021/acsami.9b23260.

Further experimental observations and results of the electrical measurements; graphs of Figure S1 showing electrical measurement data (PDF)

## ■ AUTHOR INFORMATION


### Corresponding Author

**Alex M. Lord** − *Centre for NanoHealth, College of Engineering, Swansea University, Swansea SA2 8PP, United Kingdom;* orcid.org/0000-0002-6258-2187; Email: a.m.lord@swansea.ac.uk

### Authors

**Vincent Consonni** − *Univ. Grenoble Alpes, CNRS, Grenoble INP, LMGP, F-38000 Grenoble, France;* orcid.org/0000-0003-0171-8746

**Thomas Cossuet** − *Univ. Grenoble Alpes, CNRS, Grenoble INP, LMGP, F-38000 Grenoble, France;* orcid.org/0000-0002-9398-7814

**Fabrice Donatini** − *Univ. Grenoble Alpes, CNRS, Grenoble INP, Institut NEEL, F-38000 Grenoble, France*

**Steve P. Wilks** − *Multidisciplinary Nanotechnology Centre, Department of Physics, College of Science, Swansea University, Swansea SA2 8PP, United Kingdom*

Complete contact information is available at: https://pubs.acs.org/10.1021/acsami.9b23260


### Author Contributions

The manuscript was written through contributions of all authors. All authors have given approval to the final version of the manuscript.

### Notes

The authors declare no competing financial interest.

## ■ ACKNOWLEDGMENTS

A.M.L. would like to thank the support of the Sêr Cymru II fellowship scheme partly funded by the European Regional Development Fund through the Welsh Government. This work was supported by the Centre for Nanohealth, Swansea University, U.K. Support was provided by the Engineering and Physical Sciences Research Council-funded Impact Acceleration Account (grant number EP/R511614/1). V.C. acknowledges the funding by the French Research National Agency through projects ROLLER (ANR-17-CE09-0033) and DOSETTE (ANR-17-CE24-0003). This work was partly supported by the French RENATECH network through the CIME-Nanotech and PTA technological platforms in a clean room environment. The authors thank Jean-Luc Thomassin from CEA-IRIG (Grenoble, France) for his assistance in the EBL experiments.

## ■ REFERENCES


(1) Lauritsen, J. V.; Porsgaard, S.; Rasmussen, M. K.; Jensen, M. C. R.; Bechstein, R.; Meinander, K.; Clausen, B. S.; Helveg, S.; Wahl, R.; Kresse, G.; Besenbacher, F. Stabilization Principles for Polar Surfaces of ZnO. *ACS Nano* **2011**, *5*, 5987−5994.

(2) Zúñiga-Pérez, J.; Consonni, V.; Lymperakis, L.; Kong, X.; Trampert, A.; Fernández-Garrido, S.; Brandt, O.; Renevier, H.; Keller, S.; Hestroffer, K.; Wagner, M. R.; Reparaz, J. S.; Akyol, F.; Rajan, S.; Rennesson, S.; Palacios, T.; Feuillet, G. Polarity in GaN and ZnO: Theory, Measurement, Growth, and Devices. *Appl. Phys. Rev.* **2016**, *3*, No. 041303.

(3) Heinhold, R.; Williams, G. T.; Cooil, S. P.; Evans, D. A.; Allen, M. W. Influence of Polarity and Hydroxyl Termination on the Band Bending at ZnO Surfaces. *Phys. Rev. B* **2013**, *88*, No. 235315.

(4) Brillson, L. J.; Mosbacker, H. L.; Hetzer, M. J.; Strzhemechny, Y.; Jessen, G. H.; Look, D. C.; Cantwell, G.; Zhang, J.; Song, J. J. Dominant Effect of Near-Interface Native Point Defects on ZnO Schottky Barriers. *Appl. Phys. Lett.* **2007**, *90*, No. 102116.

(5) Janotti, A.; Van de Walle, C. G. Fundamentals of Zinc Oxide as a Semiconductor. *Rep. Prog. Phys.* **2009**, *72*, No. 126501.

(6) Polyakov, A. Y.; Smirnov, N. B.; Kozhukhova, E. A.; Vdovin, V. I.; Ip, K.; Heo, Y. W.; Norton, D. P.; Pearton, S. J. Electrical Characteristics of Au and Ag Schottky Contacts on n-ZnO. *Appl. Phys. Lett.* **2003**, *83*, 1575.

(7) Consonni, V.; Sarigiannidou, E.; Appert, E.; Bocheux, A.; Guillemin, S.; Donatini, F.; Robin, I.-C.; Kioseoglou, J.; Robaut, F. Selective Area Growth of Well-Ordered ZnO Nanowire Arrays with Controllable Polarity. *ACS Nano* **2014**, *8*, 4761−4770.

(8) Espinosa, H. D.; Bernal, R. A.; Minary-Jolandan, M. Review of Mechanical and Electromechanical Properties of Piezoelectric Nanowires. *Adv. Mater.* **2012**, *24*, 4656−4675.

(9) Briscoe, J.; Dunn, S. Piezoelectric Nanogenerators - a Review of Nanostructured Piezoelectric Energy Harvesters. *Nano Energy* **2015**, *14*, 15−29.

(10) Lin, P.; Yan, X.; Zhang, Z.; Shen, Y.; Zhao, Y.; Bai, Z.; Zhang, Y. Self-Powered UV Photosensor Based on PEDOT:PSS/ZnO Micro/Nanowire with Strain-Modulated Photoresponse. *ACS Appl. Mater. Interfaces* **2013**, *5*, 3671−3676.

(11) Lu, S.; Qi, J.; Liu, S.; Zhang, Z.; Wang, Z.; Lin, P.; Liao, Q.; Liang, Q.; Zhang, Y. Piezotronic Interface Engineering on ZnO/Au-Based Schottky Junction for Enhanced Photoresponse of a Flexible Self-Powered UV Detector. *ACS Appl. Mater. Interfaces* **2014**, *6*, 14116−14122.

(12) Sallet, V.; Sartel, C.; Vilar, C.; Lusson, A.; Galtier, P. Opposite Crystal Polarities Observed in Spontaneous and Vapour-Liquid-Solid Grown ZnO Nanowires. *Appl. Phys. Lett.* **2013**, *102*, No. 182103.

(13) De La Mata, M.; Zamani, R. R.; Martí-Sánchez, S.; Eickhoff, M.; Xiong, Q.; Fontcuberta Morral, A.; Caroff, P.; Arbiol, J. The Role of Polarity in Nonplanar Semiconductor Nanostructures. *Nano Lett.* **2019**, *19*, 3396−3408.

(14) Allen, M. W.; Alkaisi, M. M.; Durbin, S. M. Metal Schottky Diodes on Zn-Polar and O-Polar Bulk ZnO. *Appl. Phys. Lett.* **2006**, *89*, No. 103520.

(15) D'Amico, N. R.; Cantele, G.; Perroni, C. A.; Ninno, D. Electronic Properties and Schottky Barriers at ZnO-Metal Interfaces from First Principles. *J. Phys.: Condens. Matter* **2015**, *27*, No. 015006.

(16) Cossuet, T.; Appert, E.; Thomassin, J.-L.; Consonni, V. Polarity-Dependent Growth Rates of Selective Area Grown ZnO Nanorods by Chemical Bath Deposition. *Langmuir* **2017**, *33*, 6269−6279.

(17) Cobley, R. J.; Brown, R. A.; Barnett, C. J.; Maffeis, T. G. G.; Penny, M. W. Quantitative Analysis of Annealed Scanning Probe Tips using Energy Dispersive X-Ray Spectroscopy. *Appl. Phys. Lett.* **2013**, *102*, No. 023111.

(18) Lord, A. M.; Ward, M. B.; Evans, J. E.; Davies, P. R.; Smith, N. A.; Maffeis, T. G.; Wilks, S. P. Enhanced Long-Path Electrical Conduction in ZnO Nanowire Array Devices Grown via Defect-Driven Nucleation. *J. Phys. Chem. C* **2014**, *118*, 21177−21184.

(19) Lord, A. M.; Maffeis, T. G.; Kryvchenkova, O.; Cobley, R. J.; Kalna, K.; Kepaptsoglou, D. M. D.; Ramasse, Q. M.; Walton, A. S.; Ward, M. B.; Köble, J.; Wilks, S. P. Controlling the Electrical Transport Properties of Nanocontacts to Nanowires. *Nano Lett.* **2015**, *15*, 4248−4254.
(20) Smith, N. A.; Lord, A. M.; Evans, J. E.; Barnett, C. J.; Cobley, R. J.; Wilks, S. P. Forming Reproducible Non-Lithographic Nanocontacts to assess the effect of Contact Compressive Strain in Nanomaterials. *Semicond. Sci. Technol.* **2015**, *30*, No. 065011.
(21) Park, W. I.; Jung, S. W.; Yi, G.-C.; Oh, S. H.; Park, C. G.; Kim, M. Metal-ZnO Heterostructure Nanorods with an Abrupt Interface. *Jpn. J. Appl. Phys.* **2002**, *41*, L1206−L1208.
(22) Rhoderick, E. H.; Williams, R. H. *Metal−Semiconductor Contacts*; Clarendon Press: Oxford, 1988.
(23) Cheung, S. K.; Cheung, N. W. Extraction of Schottky Diode Parameters from Forward Current-Voltage Characteristics. *Appl. Phys. Lett.* **1986**, *49*, 85−87.
(24) Crowell, C. R.; Rideout, V. L. Normalized Thermionic-Field (T-F) Emission in Metal-Semiconductor (Schottky) Barriers. *Solid State Electron.* **1969**, *12*, 89−105.
(25) Özgür, U.; Alivov, Y. I.; Liu, C.; Teke, A.; Reshchikov, M. A.; Doğan, S.; Avrutin, V.; Cho, S.-J.; Morkoç, H. A Comprehensive Review of ZnO Materials and Devices. *J. Appl. Phys.* **2005**, *98*, No. 041301.
(26) Tung, R. Electron Transport at Metal-Semiconductor Interfaces: General Theory. *Phys. Rev. B* **1992**, *45*, 13509−13523.
(27) Müller, S.; von Wenckstern, H.; Schmidt, F.; Splith, D.; Heinhold, R.; Allen, M.; Grundmann, M. Method of Choice for Fabrication of High-Quality ZnO-Based Schottky Diodes. *J. Appl. Phys.* **2014**, *116*, No. 194506.
(28) Cossuet, T.; Donatini, F.; Lord, A. M.; Appert, E.; Pernot, J.; Consonni, V. Polarity-Dependent High Electrical Conductivity of ZnO Nanorods and its Relation to Hydrogen. *J. Phys. Chem. C* **2018**, *122*, 22767−22775.
(29) Lord, A. M.; Evans, J. E.; Barnett, C. J.; Allen, M. W.; Barron, A. R.; Wilks, S. P. Surface Sensitivity of Four-Probe STM Resistivity Measurements of Bulk ZnO Correlated to XPS. *J. Phys.: Condens. Matter* **2017**, *29*, No. 384001.
(30) Polyakov, A. Y.; Smirnov, N. B.; Govorkov, A. V.; Ip, K.; Overberg, M. E.; Heo, Y. W.; Norton, D. P.; Pearton, S. J.; Luo, B.; Ren, F.; Zavada, J. M. Hydrogen Plasma Treatment Effects on Electrical and Optical Properties of *n* -ZnO. *J. Appl. Phys.* **2003**, *94*, 400−406.
(31) Allen, M. W.; Durbin, S. M. Influence of Oxygen Vacancies on Schottky Contacts to ZnO. *Appl. Phys. Lett.* **2008**, *92*, No. 122110.
(32) Müller, S.; von Wenckstern, H.; Schmidt, F.; Splith, D.; Schein, F.-L.; Frenzel, H.; Grundmann, M. Comparison of Schottky Contacts on *β*-Gallium Oxide Thin Films and Bulk Crystals. *Appl. Phys. Express* **2015**, *8*, No. 121102.
(33) Léonard, F.; Talin, A.; Swartzentruber, B.; Picraux, S. Diameter-Dependent Electronic Transport Properties of Au-Catalyst/Ge-Nanowire Schottky Diodes. *Phys. Rev. Lett.* **2009**, *102*, No. 106805.
(34) Smit, G.; Rogge, S.; Caro, J.; Klapwijk, T. Conductance Distribution in Nanometer-Sized Semiconductor Devices due to Dopant Statistics. *Phys. Rev. B* **2004**, *69*, No. 035338.
(35) Roy, A. M.; Lin, J. Y. J.; Saraswat, K. C. Specific Contact Resistivity of Tunnel Barrier Contacts used for Fermi Level Depinning. *IEEE Electron Device Lett.* **2010**, *31*, 1077−1079.
(36) Sett, S.; Das, K.; Raychaudhuri, A. K. Investigation of Factors Affecting Electrical Contacts on Single Germanium Nanowires. *J. Appl. Phys.* **2017**, *121*, No. 124503.
(37) Yu, A. Y. C. Electron Tunneling and Contact Resistance of Metal-Silicon Contact Barriers. *Solid State Electron.* **1970**, *13*, 239−247.
(38) Mosbacker, H. L.; Strzhemechny, Y. M.; White, B. D.; Smith, P. E.; Look, D. C.; Reynolds, D. C.; Litton, C. W.; Brillson, L. J. Role of Near-Surface States in Ohmic-Schottky Conversion of Au Contacts to ZnO. *Appl. Phys. Lett.* **2005**, *87*, No. 012102.
(39) Coppa, B. J.; Davis, R. F.; Nemanich, R. J. Gold Schottky Contacts on Oxygen Plasma-Treated, n-type ZnO(0001-bar). *Appl. Phys. Lett.* **2003**, *82*, 400−402.
(40) Cox, J. W.; Foster, G. M.; Jarjour, A.; von Wenckstern, H.; Grundmann, M.; Brillson, L. J. Defect Manipulation to Control ZnO Micro-/Nanowire-Metal Contacts. *Nano Lett.* **2018**, *18*, 6974−6980.
(41) Foster, G. M.; Gao, H.; Mackessy, G.; Hyland, A. M.; Allen, M. W.; Wang, B.; Look, D. C.; Brillson, L. J. Impact of Defect Distribution on IrO x /ZnO Interface Doping and Schottky Barriers. *Appl. Phys. Lett.* **2017**, *111*, No. 101604.
(42) Allen, M. W.; Mendelsberg, R. J.; Reeves, R. J.; Durbin, S. M. Oxidized Noble Metal Schottky Contacts to n-type ZnO. *Appl. Phys. Lett.* **2009**, *94*, No. 103508.
(43) Montenegro, D. N.; Hortelano, V.; Martínez, O.; Martínez-Tomas, M. C.; Sallet, V.; Muñoz-Sanjosé, V.; Jiménez, J. Non-Radiative Recombination Centres in Catalyst-Free ZnO Nanorods Grown by Atmospheric-Metal Organic Chemical Vapour Deposition. *J. Phys. D: Appl. Phys.* **2013**, *46*, No. 235302.
(44) Lavrov, E. V.; Herklotz, F.; Weber, J. Identification of Two Hydrogen Donors in ZnO. *Phys. Rev. B* **2009**, *79*, No. 165210.
(45) Heinhold, R.; Neiman, A.; Kennedy, J. V.; Markwitz, A.; Reeves, R. J.; Allen, M. W. Hydrogen-Related Excitons and their Excited-State Transitions in ZnO. *Phys. Rev. B* **2017**, *95*, No. 054120.
(46) Meyer, B. K.; Alves, H.; Hofmann, D. M.; Kriegseis, W.; Forster, D.; Bertram, F.; Christen, J.; Hoffmann, A.; Straßburg, M.; Dworzak, M.; Haboeck, U.; Rodina, A. V. Bound Exciton and Donor−Acceptor Pair Recombinations in ZnO. *Phys. Status Solidi B* **2004**, *241*, 231−260.
(47) Janotti, A.; Van De Walle, C. G. Native Point Defects in ZnO. *Phys. Rev. B* **2007**, *76*, No. 165202.
(48) Lyons, J. L.; Varley, J. B.; Steiauf, D.; Janotti, A.; Van De Walle, C. G. First-principles Characterization of Native-Defect-Related Optical Transitions in ZnO. *J. Appl. Phys.* **2017**, *122*, No. 035704.
(49) Frodason, Y. K.; Johansen, K. M.; Bjørheim, T. S.; Svensson, B. G.; Alkauskas, A. Zn Vacancy-Donor Impurity Complexes in ZnO. *Phys. Rev. B* **2018**, *97*, No. 104109.
(50) Vanheusden, K.; Warren, W. L.; Seager, C. H.; Tallant, D. R.; Voigt, J. A.; Gnade, B. E. Mechanisms behind Green Photoluminescence in ZnO Phosphor Powders. *J. Appl. Phys.* **1996**, *79*, 7983−7990.
(51) Reynolds, D. C.; Look, D. C.; Jogai, B.; Van Nostrand, J. E.; Jones, R.; Jenny, J. Source of the Yellow Luminescence Band in GaN Grown by Gas-Source Molecular Beam Epitaxy and the Green Luminescence Band in Single Crystal ZnO. *Solid State Commun.* **1998**, *106*, 701−704.
(52) Van de Walle, C. G. Hydrogen as a cause of Doping in Zinc Oxide. *Phys. Rev. Lett.* **2000**, *85*, 1012−1015.
(53) Herklotz, F.; Hupfer, A.; Johansen, K. M.; Svensson, B. G.; Koch, S. G.; Lavrov, E. V. Infrared Absorption on a Complex Comprising Three Equivalent Hydrogen Atoms in ZnO. *Phys. Rev. B* **2015**, *92*, No. 155203.
(54) Lavrov, E. V.; Herklotz, F.; Weber, J. Identification of Hydrogen Molecules in ZnO. *Phys. Rev. Lett.* **2009**, *102*, No. 185502.
(55) Kennedy, O. W.; White, E. R.; Howkins, A.; Williams, C. K.; Boyd, I. W.; Warburton, P. A.; Shaffer, M. S. P. Mapping the Origins of Luminescence in ZnO Nanowires by STEM-CL. *J. Phys. Chem. Lett.* **2019**, *10*, 386−392.
(56) Li, H.; Saito, M.; Chen, C.; Inoue, K.; Akagi, K.; Ikuhara, Y. Strong Metal−Metal Interaction and Bonding Nature in Metal/Oxide Interfaces with Large Mismatches. *Acta Mater.* **2019**, *179*, 237−246.
(57) Berthod, C.; Binggeli, N.; Baldereschi, A. Schottky Barrier Heights at Polar Metal/Semiconductor Interfaces. *Phys. Rev. B* **2003**, *68*, No. 085323.
(58) Ton-That, C.; Lem, L. L. C.; Phillips, M. R.; Reisdorffer, F.; Mevellec, J.; Nguyen, T. P.; Nenstiel, C.; Hoffmann, A. Shallow Carrier Traps in Hydrothermal ZnO Crystals. *New J. Phys.* **2014**, *16*, No. 083040.
(59) Penfold, T. J.; Szlachetko, J.; Santomauro, F. G.; Britz, A.; Gawelda, W.; Doumy, G.; March, A. M.; Southworth, S. H.;


https://dx.doi.org/10.1021/acsami.9b23260
ACS Appl. Mater. Interfaces 2020, 12, 13217−13228

Rittmann, J.; Abela, R.; Chergui, M.; Milne, C. J. Revealing Hole Trapping in Zinc Oxide Nanoparticles by Time-Resolved X-Ray Spectroscopy. *Nat. Commun.* **2018**, *9*, No. 478.
(60) Li, M.; Xing, G.; Xing, G.; Wu, B.; Wu, T.; Zhang, X.; Sum, T. C. Origin of Green Emission and Charge Trapping Dynamics in ZnO Nanowires. *Phys. Rev. B* **2013**, *87*, No. 115309.
(61) Diebold, U.; Koplitz, L. V.; Dulub, O. Atomic-Scale Properties of Low-Index ZnO Surfaces. *Appl. Surf. Sci.* **2004**, *237*, 336−342.



https://dx.doi.org/10.1021/acsami.9b23260
*ACS Appl. Mater. Interfaces* 2020, 12, 13217−13228